

## Article

# A Deep Learning-Based Approach to Predict Large-Scale Dynamics of Normalized Difference Vegetation Index for the Monitoring of Vegetation Activities and Stresses Using Meteorological Data

Ying Sun <sup>1</sup>, Dazhao Lao <sup>2</sup>, Yongjian Ruan <sup>3</sup>, Chen Huang <sup>1</sup> and Qinchuan Xin <sup>1,4,\*</sup>

<sup>1</sup> School of Geography and Planning, Guangdong Key Laboratory for Urbanization and Geo-Simulation, Sun Yat-Sen University, Guangzhou 510275, China

<sup>2</sup> Tandon School of Engineering, New York University, Brooklyn, New York, NY 11201, USA

<sup>3</sup> School of Geographical Science, Guangzhou University, Guangzhou 510006, China

<sup>4</sup> State Key Laboratory of Desert and Oasis Ecology, Research Center for Ecology and Environment of Central Asia, Chinese Academy of Sciences, Urumqi 830011, China

\* Correspondence: xinqinchuan@mail.sysu.edu.cn

**Abstract:** Vegetation activities and stresses are crucial for vegetation health assessment. Changes in an environment such as drought do not always result in vegetation drought stress as vegetation responses to the climate involve complex processes. Satellite-based vegetation indices such as the Normalized Difference Vegetation Index (NDVI) have been widely used to monitor vegetation activities. As satellites only carry information for understanding past and current vegetation conditions, there is a need to model vegetation dynamics to make future predictions. Although many other factors are related, we attempt to predict the vegetation activities and stresses via simulating NDVI, based on only meteorological data and using a deep learning method (bidirectional long short-term memory model, BiLSTM). The BiLSTM is a sequence processing model that can predict NDVI by establishing the relationship between meteorological variables and vegetation activities. Experimental results show that the predicted NDVI is consistent with the reference data ( $R^2 = 0.69 \pm 0.28$ ). The best accuracy was achieved in the deciduous forest ( $R^2 = 0.87 \pm 0.16$ ). The vegetation condition index (VCI) calculated from the BiLSTM-predicted NDVI also agreed with the satellite-based ones ( $R^2 = 0.70 \pm 0.28$ ). Both the monitored and predicted VCI indicated an upward but insignificant trend of vegetation activity in the past decade and increased vegetation stresses in the early growing season over northern China. Based on meteorological data, the deep learning-based solution shows the potential for not only retrospective analysis, but also future prediction of vegetation activities and stresses under varied climate conditions as compared with remote sensing data.

**Keywords:** NDVI time series; meteorological data; deep learning; BiLSTM; vegetation activities and stresses; prediction



**Citation:** Sun, Y.; Lao, D.; Ruan, Y.; Huang, C.; Xin, Q. A Deep Learning-Based Approach to Predict Large-Scale Dynamics of Normalized Difference Vegetation Index for the Monitoring of Vegetation Activities and Stresses Using Meteorological Data. *Sustainability* **2023**, *15*, 6632. <https://doi.org/10.3390/su15086632>

Academic Editor: Hong Tang

Received: 8 February 2023

Revised: 18 March 2023

Accepted: 6 April 2023

Published: 13 April 2023



**Copyright:** © 2023 by the authors. Licensee MDPI, Basel, Switzerland. This article is an open access article distributed under the terms and conditions of the Creative Commons Attribution (CC BY) license (<https://creativecommons.org/licenses/by/4.0/>).

## 1. Introduction

Ongoing climate change has intensified droughts in particular regions [1]. Climatic drought is the main influence factor of vegetation activities, affecting vegetation health, ecosystem function, water cycle, soil, and agricultural production [2–4]. The available satellite images make the monitoring of vegetation easier owing to data collection over large geographical areas within short revisit intervals [5]. Vegetation indices (VIs) derived from remote sensing data are indicative of vegetation activities or stresses on the land surface [6–8].

Various vegetation indices (VIs) have been defined by the combination of surface reflectance at two or more wavelengths [7], such as the Normalized Difference Vegetation Index (NDVI) [9], Green Normalized Difference Vegetation Index (GNDVI) [10], Red Edge Normalized Difference Vegetation Index (RENDVI) [11], Soil-Adjusted Vegetation

Index (SAVI) [12], and Enhanced Vegetation Index (EVI) [13]. Based on a similar principle, these VIs employ near-infrared band (NIR) and the band in the effective spectral range of photosynthesis to derive information related to vegetation. Among the available indices, NDVI is one of the most widely acknowledged and frequently used indices for monitoring vegetation activities [14]. The generalized NDVI time series of vegetation often has a seasonal cycle that is correspondent to activities such as plant growth and senescence [15]. NDVI time series at high temporal resolution provides a trajectory of vegetation activities and are useful for monitoring and detecting changes in vegetation conditions and dynamics [7,16]. Ali et al. [8] studied the impact of drought on China's vegetation based on the NDVI derived from AVHRR, and temperature and precipitation data from NASA's MERRA. Zhao et al. [17] modified the comprehensive remote sensing drought indices and analyze the spatial-temporal patterns of drought in China from 1982–2010. Jiang et al. [18] employed the meteorological data-based index (SPEI) and remotely sensed derived NDVI to investigate the drought activity as well as the relationship between drought and vegetation in Northwest China. For better vegetation activity monitoring, Kogan [19] proposed vegetation condition index (VCI) to filter out these nonweather effects by using geographic filtering. VCI enhanced weather-related impacts compared with NDVI, and has been extensively used for monitoring vegetation activity. Liang et al. [20] used VCI for the analysis of vegetative drought conditions in China based on NOAA/AVHRR. Satellite-based drought indices [21] have been proved to be effective and convenient in detecting drought conditions at regional and global scales.

While satellite-derived VIs have been found useful on retrospective studies and near real-time monitoring of vegetation activities on the land surface, bad weather or cloud pose a challenge for satellite remote sensing because they lead to missing data in the time series [22]. It is a critical problem that limits the availability of usable images for continuous fine-grained vegetation dynamics monitoring [23] and, what's more, they cannot make future predictions. There is a need to improve our abilities of modeling and predicting on VIs when satellite observations were and are not available.

Vegetation activities are controlled by a changing environment on spatial and temporal scales [24]. Although the meteorological droughts do not always result in decreases in NDVI, meteorological data—such as temperature and precipitation—are important factors of climatic determinants that affect vegetation activities [25]. Climate variables are monitored day by day without data-missing issues. The Intergovernmental Panel on Climate Change (IPCC) also presented the Shared Socio-Economic Paths (SSP) dataset that can offer future climate scenarios. In land surface studies, it is an important goal to model vegetation activities via climate variables. The past and future meteorological data at high temporal and spatial resolutions are useful for understanding and predicting vegetation activity dynamics. Gao, Jiao, Wu, Ma, Zhao, Yin and Dai [2] employed a geographically weighted regression (GWR) model which is based on climate observation (temperature and precipitation) for net primary productivity (NPP) simulation. Wang et al. [26] analyzed NPP changes in China based on 11 earth system models under 4 RCPs. Recently, Zheng et al. [27] proposed a series of pixel-based Vegetation Dynamics Stepwise-cluster Prediction models (VEDSP) to simulate NDVI via climate conditions. Zhou et al. [28] developed a multi-regression prediction model for dynamic changes of vegetation in China, based on meteorological data and NDVI. Barrett et al. [29] applied linear autoregression and Gaussian process modelling methods to forecast NDVI based on MODIS and Landsat data. Although many other factors, such as soil and elevation, influence vegetation activities [30], we attempt to investigate the ability of meteorological data for the NDVI time series simulation.

Different from empirical or numerical methods, machine learning methods have gained increasing attention in land surface modeling studies [31,32]. Convolutional neural networks (CNNs) are able to learn the functional relationships between independent and dependent variables. CNNs provide a hierarchical representation of the input data using a stack of convolutional layers, and are suitable for handling large volume data over

long time series [33]. Considering these advantages of CNNs, some studies have used it for NDVI prediction. Das and Ghosh [34] proposed a deep CNN (Deep-STEP) derived from the original deep stacking network for predicting NDVI, and validated the results on Landsat-7 NDVI time series over four regions in India. Mazza, Gargiulo, Scarpa and Gaetano [23] proposed a common CNN-based data fusion method to simulate the NDVI from coupled Sentinel1-1 and Sentinel1-2 time series. The time series used in CNNs is beneficial in the NDVI simulation as it is evaluated using spatial data; however, because CNNs do not extract and use temporal information, the knowledge in the time series is missing when using CNNs [5,22]. Recurrent neural networks (RNNs) with various dynamic models are deep in time and are often used in sequence processing, such as music and text generation [35]. To address this shortcoming, Stepchenko and Chizhov [7] used RNNs for predicting the NDVI time series using input data from a multi-temporal smoothed MODIS NDVI time series. Whereas RNNs often suffer from memory compression that can impact the ability of long-range sequence information memory [36], as well as the vanishing gradient effect that can result in error back-propagation over a long temporal interval [37], long short-term memory (LSTM), first proposed by [38], is a variant of RNN architecture that can memorize and forget the long-range temporal information based on the LSTM units. According to the literature, LSTM is an excellent method for sequence-related tasks, such as activity recognition, video description, and language translation [39]. LSTMs have gained particular attention in land use and land cover [40]. The work of Reddy and Prasad [5] provides an example of using the LSTM model to predict vegetation dynamics based on MODIS NDVI time series data in a small evergreen forest in India. In the field of vegetation activity monitoring, the application of LSTM is still at a nascent stage.

Motivated by the above context, this study investigates the ability of the LSTM architecture to predict the NDVI time series for each vegetation type, based only on meteorological data. Compared with satellite remote sensing data, the deep learning-based model can be used for both monitoring and predicting vegetation activities. In this study, a bidirectional LSTM was developed to match the meteorological data and NDVI time series from both directions, and was used to predict NDVI. To illustrate the usefulness of our modeling approach, we further identify and compare the vegetation stresses over China during the period of 2009–2017, based on VCI derived from both predicted and observed NDVI.

## 2. Study Area and Materials

### 2.1. Study Area

With multiple climate regimes and diverse topographies, China covers almost all vegetation types in the northern hemisphere (Figure 1). According to temperature distribution, we divided China into five temperate climate zones with different vegetation types [41]. In China, coniferous forests are mainly distributed in the East humid zone, ranging from cold temperate zone, temperate zone to subtropical zone. In addition, China is rich in broad-leaved forests, which are often mixed with coniferous forests in temperate and warm temperate zones, and are often evergreen in subtropical and tropical zones. Grasslands cover large areas in China and are primarily distributed in the temperate zone from northeast to northwest. Woody savannas and savannas are mainly scattered in the warm temperate and subtropical zones. Croplands are mainly present in the central and eastern coastal areas from the temperate to the tropical zones [42]. During the past few decades, ecosystems in China have been influenced by climate change and human activities such as urbanization and agricultural practices [43].

### 2.2. Meteorological Data

The meteorological data used in this study were collected from the China Meteorological Administration (CMA) land data assimilation system (CLDAS) 2.0. CLDAS 2.0 is an hourly air drive field product with a spatial resolution of  $0.0625^\circ \times 0.0625^\circ$  covering Asia ( $0^\circ$ – $65^\circ$  N,  $60^\circ$ – $160^\circ$  E). CLDAS 2.0 provided data for six variables, including 2-m air temperature, atmospheric pressure, humidity, 10-m wind speed, precipitation, and

incoming shortwave radiation. For the NDVI simulation, we selected atmospheric pressure, precipitation, and incoming shortwave radiation from CLDAS 2.0, and averaged hourly data to daily data. We derived the daily maximum and minimum air temperatures from hourly air temperature. In addition, we calculated the day length of each pixel in the study area according to the method described by Amthor [44]. In summary, six daily variables, including atmospheric pressure, precipitation, incoming shortwave radiation, maximum air temperature, minimum air temperature, and day length, were used as the model inputs. The meteorological time series data were derived for the time period spanning from 1 January 2008 to 31 December 2017.

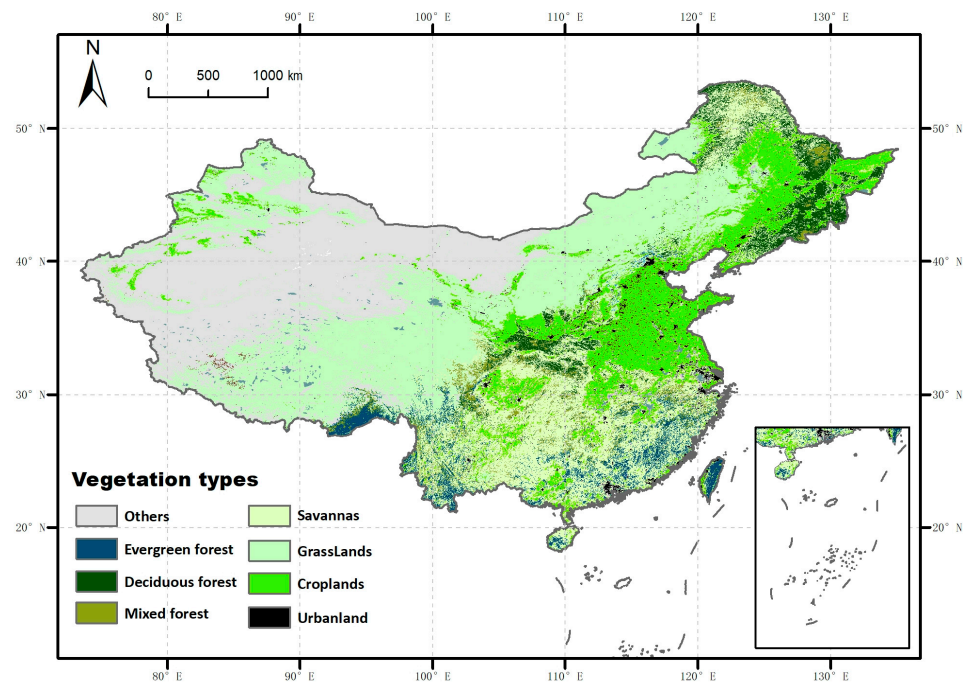


**Figure 1.** The study area of China that includes various vegetation types.

### 2.3. Remote Sensing Data and Preprocessing

We used the land surface reflectance product of MOD09A1 [45] based on MODIS for calculating NDVI [9]. MOD09A1 provides 8-day gridded Level-3 land surface reflectance data at 500-m spatial resolution. The surface reflectance data for MOD09A1 were derived based on the MODIS Level1B products. Each pixel is assigned the best value every 8 days according to factors such as cloud cover and solar azimuth. The 8-day NDVI time series were derived from MOD09A1 using data from the NIR band and the visible band according to Equation (1). We used high-quality bands to ensure data quality. NDVI varies from  $-1.0$  to  $1.0$  in vegetated areas. NDVI is generally greater than 0.

$$NDVI = (Band_{NIR} - Band_{RED}) / (Band_{NIR} + Band_{RED}), \quad (1)$$

We reconstructed the 8-day time series of NDVI to reduce the noise originating from sensors, weather, and other reasons. We smoothed the 8-day NDVI using the Savitzky–Golay filtering method [46] to remove spikes in the time series mostly caused by environmental factors such as clouds and rain. We then linearly interpolated the smoothed 8-day NDVI to obtain daily NDVI for an entire year.

We used the MODIS annual land cover product of MCD12Q1 with a spatial resolution of 500 m for land cover extraction [47]. We used the land cover data based on the International Geosphere-Biosphere Programme (IGBP) classification system [48], which classifies the land surface into 17 categories, including 11 types of natural vegetation, 3 types of land use and land cover mosaic, and 3 types of non-vegetation. According to the purpose of this study, the 11 natural vegetation types were merged into 7 classes: deciduous forests,

evergreen forests, mixed forests, shrublands, grasslands, savannas, and croplands. Because there are only small areas of shrublands in China, we selected the remaining six types, including deciduous forests, evergreen forests, mixed forests, grasslands, savannas, and croplands, for study. To match the input and output of the deep learning model, both the preprocessed NDVI data and the land cover data were reprojected and resampled to make them consistent with the meteorological data. The meteorological data are masked by pixels of the above six vegetation types to serve as the BiLSTM model input.

### 3. Methodology

#### 3.1. Simulation of NDVI Using Vegetation-Type-Based BiLSTM (NDVI-BiLSTM)

##### 3.1.1. An Overview of Vegetation-Type-Based NDVI-BiLSTM

The proposed architecture of the BiLSTM model for NDVI simulation based on meteorological time series data for each vegetation type mainly consists of five layers and is derived from LSTM (Figure 2) [49]. Two BiLSTM layers are employed to compute the output sequence by iterating the forward and backward LSTM cells using the input sequence. The first BiLSTM layer transfers all hidden states ( $\vec{h}_t, \overleftarrow{h}_t$ ) to the dropout layer. The hidden states  $\vec{h}_t$  extracts features from the forward sequence of time series (Blue right arrow in Figure 2), while  $\overleftarrow{h}_t$  extracts features from the inverse sequence of time series (Blue left arrow in Figure 2). This dropout layer can discard the neural network unit temporally, which can reduce the parameters and prevent overfitting. After these processes, the BN layer normalizes the transferred features to avoid internal covariate shift and the resulting vanishing gradients. The normalized features are transferred to the second BiLSTM layer to compute the representation ( $\vec{h}_t, \overleftarrow{h}_t$ ) of the sequence. The dense layer is a standard one-dimensional fully connected layer. The representations given by the last hidden state of the BiLSTM layer are then forwarded to the dense layer to form a one-dimensional vector. Finally, the activation layer controls the activation level of the neuron for the forward signal transformation and generates the outputs, that is, the predicted NDVI time series.

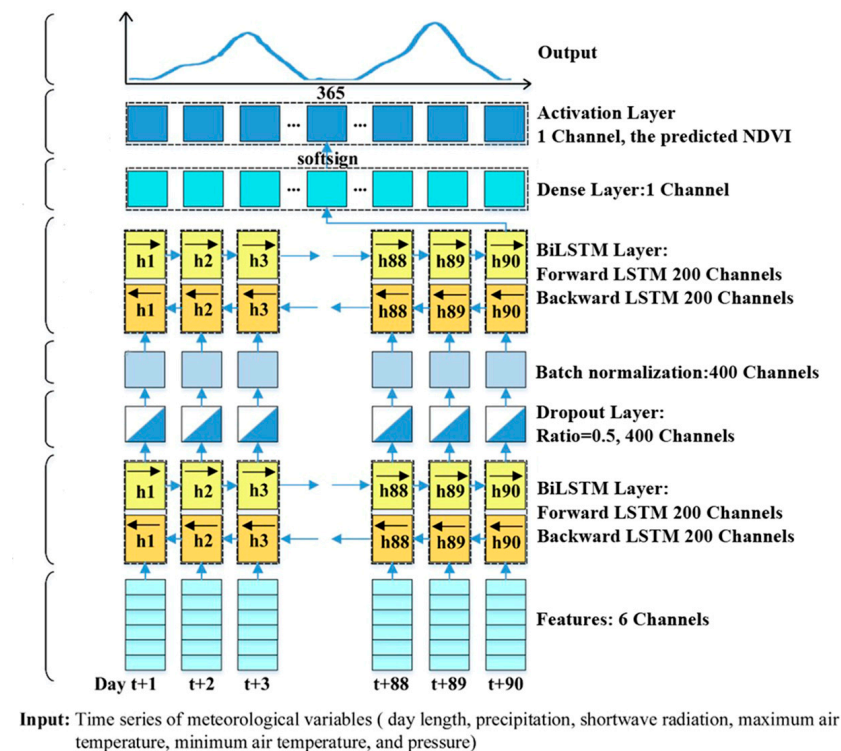
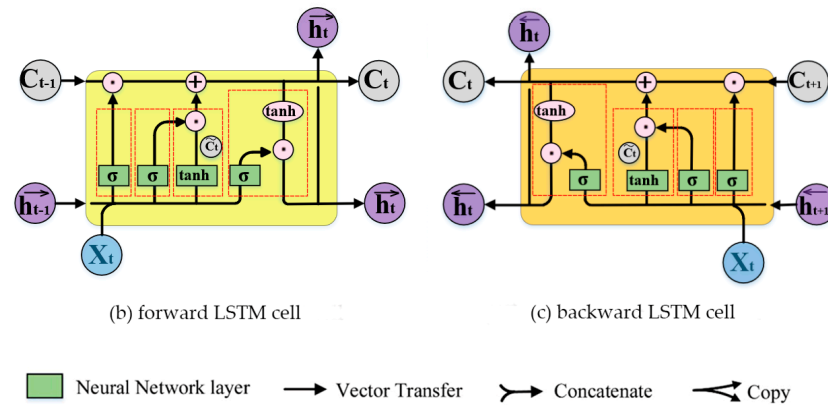


Figure 2. Cont.



**Figure 2.** (a) The architecture of the deep learning model of NDVI-BiLSTM, which is derived from Graves, et al. [50] and Hochreiter and Schmidhuber [38]. The bidirectional LSTM cells are employed in NDVI simulation, and (b) for forward LSTM cell and (c) for backward LSTM cell. (Reprinted with permission from Ref. [50] and Ref. [38], Copyright 2013, IEEE and Copyright 1997, Massachusetts Institute of Technology). Take the forward LSTM cell as example, the previous hidden state  $h_{t-1}$  for the current cell state  $C_t$  and the current input  $X_t$  are concatenated for feature extraction using the four neural network layers (three gates). The features are then transferred forward. In a branch, the features are used to update the current cell state  $C_t$ . In the other branch, the features are copied to transferred into the next BiLSTM layer and the next day (time sequence).

The LSTM cell is an important component in the NDVI-BiLSTM model. The hidden units are a special gate unit in the LSTM cell, which includes three gates: the forget gate, input gate and output gate, denoted by four red dashed boxes from left to right in the forward LSTM cell in Figure 2. The hidden unit  $h_k \in \mathbb{R}^N$  learns features from sequence by incorporating the three gates incrementally, which is the short-term memory. In the case of forward LSTM at the  $k$ th day in sequence  $n$ , the forget gate  $f_k \in \mathbb{R}^N$  learns to forget some features in the previous hidden state  $h_{k-1}$  for the current cell state  $C_k$  computation (Equation (2a)). In addition, the input gate  $i_k \in \mathbb{R}^N$  and the current memory  $\tilde{C}_k \in \mathbb{R}^N$  learn to reserve useful features in the current input  $X_{tk}$  for the current cell state  $C_k$  computation (Equations (2b,c)). The output gate  $o_k \in \mathbb{R}^N$  learns to update the new hidden state  $h_k$  based on the current cell state  $C_k$  (Equations (2d,e)).

$$\left\{ \begin{array}{l} f_k = \sigma(W_f \cdot [h_{k-1}, X_k] + b_f) \quad (2a) \\ \begin{bmatrix} i_k \\ \tilde{C}_k \end{bmatrix} = \begin{bmatrix} \sigma \\ \tanh \end{bmatrix} (W_i \cdot [h_{k-1}, X_k] + b_i) \quad (2b) \\ C_k = f_k \odot C_{k-1} + i_k \odot \tilde{C}_k \quad (2c) \\ o_k = \sigma(W_o \cdot [h_{k-1}, X_k] + b_o) \quad (2d) \\ h_k = o_k \odot \tanh(C_k) \quad (2e) \end{array} \right. \quad (2)$$

where  $\sigma(x)$  is a sigmoid nonlinearity that can squash the inputs to the range of  $[0, 1]$  and  $\sigma(x) = 1/(1 + e^{-x})$ .  $W$  and  $b$  are the filter and bias, respectively.  $\tanh(x)$  is a hyperbolic tangent nonlinearity with an output range of  $[-1, 1]$ , and  $\tanh(x) = (e^x - e^{-x})/(e^x + e^{-x})$ .  $\odot$  denotes the element-wise product.  $\tilde{C}_k$  is the current memory.  $W_o$ ,  $W_i$ , and  $W_f$  denote the weights of the output gate, input gate and forget gate, respectively.

Predicting NDVI using a deep learning model is essentially a regression problem, and we employ mean square error (MSE) as the loss function:

$$Loss_{MSE} = - \sum_{i=1}^n (y_i - y'_i)^2 / n, \quad (3)$$

where  $n$  is the mini-batch size (i.e., the number of input sequences), and  $y_i$  and  $y'_i$  denote the reference and estimated NDVI values, respectively.

The computation of the backward LSTM is similar to that of the forward LSTM but at different sequences, where the input sequence for forward LSTM is  $(h_1, h_2, \dots, h_n)$  and the output sequence for backward LSTM is  $(h_n, h_{n-1}, \dots, h_1)$ .

### 3.1.2. Modeling NDVI with Vegetation-Based BiLSTM

Vegetation activity varies across land cover types, and annual NDVI fluctuation is markedly different for different vegetation types [51]. Therefore, we trained models for each vegetation type separately to predict the NDVI time series. For each vegetation type, the task is to predict the NDVI time series by establishing the relationship between meteorological variables and vegetation activities [52]. Given a time series of meteorological data  $M = (X_{1,1}, \dots, X_{1,t}, X_{2,1}, \dots, X_{2,t}, \dots, X_{m,1}, \dots, X_{m,t})$ , our NDVI-BiLSTM model estimates  $(y_1, \dots, y_{T'})$ , that is, the NDVI sequence for one vegetation type corresponding to  $1 \sim T'$  days. The input time series  $(X_{1,1}, \dots, X_{1,t}, X_{2,1}, \dots, X_{2,t}, \dots, X_{m,1}, \dots, X_{m,t})$  consists of  $m$  training pixels. Each pixel has  $t$  sequences of meteorological variables, and each sequence is expressed as  $X = (x_1, \dots, x_n)$ , where  $n$  is the length of a sequence. In this study, 500 pixels for each vegetation type were used for training. Every 90-day meteorological variable at one pixel was used to form a sequence.  $t$  is the number of sequences for one pixel, which depends on the given period  $T$ , the length of a sequence  $n$ , and the time step  $s$  in a sequence:

$$t = (T - n + 1) / s, \quad (4)$$

To predict an integral NDVI time series for a year, that is,  $t = 365$ , we set  $T = 454$ ,  $n = 90$ , and  $s = 1$ . Accordingly, the number of training data points is  $m \times t$  for each vegetation type.

Modeling NDVI with BiLSTM is a “Sequential input, static output” learning task, that is,  $(x_{t+1}, \dots, x_{t+90}) \mapsto y_{t+91}$ . With the meteorological variables of length 90 ( $t + 1 \rightarrow t + 90$ ) as input, the goal is to predict a single NDVI value at day  $t + 91$ . We use a fusion approach that uses meteorological time series data  $(x_{t+1}, \dots, x_{t+90})$  progressively to merge the single-day predicted NDVI value into the full sequence of a year. The experimental codes are available at <https://github.com/sunying23/vegetation-BiLSTM> (accessed on 5 April 2023).

### 3.1.3. Training Details

Our model is implemented using Keras [53], an application programmer’s interface on top of TensorFlow, on an NVIDIA GTX Titan GPU. We use a base learning rate of 0.01, and the learning rate is updated using Equation (5) epoch by epoch.

$$lr_i = 0.01 * (1 - i/50)^{0.6}, \quad (5)$$

where  $i$  denotes the  $i$ th epoch.

As mentioned above, 500 training samples were randomly selected for each vegetation type. In total, 3000 samples were employed for model training. We conducted two kinds of model tests from two perspectives. First, we randomly selected 20 test samples for each vegetation type from the remaining pixels (except for the 500 training samples). Second, all the remaining pixels were used for the model test in China. We trained the NDVI-BiLSTM model with back-propagation over time for a total of 100 epochs, and a mini-batch size of 64 was applied. We use the default initialization method in Keras for parameter initialization with a uniform distribution. We use MSE as the loss function to be minimized by the Adam optimizer. Dropout (Srivastava et al., 2014) [54] with a ratio of 0.5 was applied to the first BiLSTM layer. In terms of the activation layer, we used the softsign activation function (Equation (6)) to train the six studied vegetation types separately.

$$\text{softsign}(x) = \frac{x}{1 + |x|}, \quad (6)$$

### 3.2. VCI for Monitoring Vegetation Stress

NDVI is considered to have spatial variability related to the weather, vegetation type, or topography of a region [33], of which the latter two are local resource background and nonweather factors. For example, dense tropical forests and deserts have markedly different local resource backgrounds as well as NDVI values. Kogan [19] proposed VCI to filter out these nonweather effects by using geographic filtering, which is widely used in vegetation activity monitoring. Assuming that maximum NDVI is developed in years with optimal weather (non-drought years) and minimum NDVI is developed in years with unfavorable weather (drought years), for each pixel  $i$  and each week  $w$ , VCI is defined as:

$$VCI_i^w = 100 * (NDVI_i^w - NDVI_{i,min}^p) / (NDVI_{i,max}^p - NDVI_{i,min}^p), \quad (7)$$

where  $NDVI_i^w$  is the weekly NDVI of pixel  $i$ ,  $NDVI_{i,max}^p$  and  $NDVI_{i,min}^p$  are the absolute maximum and minimum NDVI for pixel  $i$  during a given period, respectively.

In this study, during the study period of 2009–2017, all pixels of different vegetation types were included for VCI computation. As shown in Equation (7), VCI varies from 0 to 100. We used three ranges to reflect vegetation conditions [55], that is, 0–40 (in stress), 40–60 (normal), and 60–100 (favorable weather).

### 3.3. Trend Analysis of Vegetation Activity in China

Many studies have used the linear regression method for trend analysis; however, it requires the normal distribution of data that are easily affected by noise. Sen's slope [56] is a trend calculation method that uses the median value of the time series, which can effectively reduce the noise. The Mann–Kendall (MK) [57,58] method allows for testing the significance of a trend in the time series. In this study, we employed Sen's slope and MK method [59] for analyzing the vegetation activity trend.

Given a time series  $V_t = (v_1, v_2, \dots, v_n)$ , Sen's slope is defined as:

$$slope = Median \left( \frac{X_j - X_k}{j - k} \right) \forall 1 < k < j < n, \quad (8)$$

$$\begin{cases} H = \sum_{i=1}^{n-1} \sum_{j=i+1}^n sgn(v_j - v_i), \text{ and} & (9-1) \\ sgn(v_j - v_i) = \begin{cases} 1, & \text{if } v_j - v_i > 0 \\ 0, & \text{if } v_j - v_i = 0 \\ -1, & \text{if } v_j - v_i < 0 \end{cases} & (9-2) \end{cases}, \quad (9)$$

where  $n$  is the number of data in the time series,  $j > i$ .

When  $n > 10$ , the MK statistic value is derived as follows:

$$MK_H = \begin{cases} \frac{H-1}{\sqrt{Var(H)}}, & \text{if } H > 0 \\ 0, & \text{if } H = 0 \\ \frac{H+1}{\sqrt{Var(H)}}, & \text{if } H < 0 \end{cases}, \quad (10)$$

$$Var(H) = \frac{n(n-1)(2n+5) - \sum_{i=1}^m t_i(t_i-1)(2t_i+5)}{18}, \quad (11)$$

where  $m$  is the number of tied values, and  $t_i$  denotes the number of ties of  $i$ th value.

Given a significant level, the slope and MK jointly determine vegetation activity trends. In this study, we used  $\alpha = 0.05$ ,  $MK_{1-\alpha/2} = MK_{0.975} = 1.96$ . Therefore, when the Sen's slope  $> 0$  and  $|MK| > 1.96$ , the sequence showed an upward trend, that is, vegetation showed marked improvement; when the Sen's slope  $> 0$  and  $|MK| \leq 1.96$ , the sequence showed an upward but insignificant trend, that is, the vegetation showed a slight improvement. Similarly, when the Sen's slope  $< 0$  and  $|MK| > 1.96$ , the sequence showed a significant downward trend, that is, the vegetation showed marked degradation; when

the Sen's slope  $< 0$  and  $|MK| \leq 1.96$ , the sequence showed a downward but insignificant trend, that is, vegetation showed slight degradation.

### 3.4. Performance Assessment

For assessment, the NDVI predicted from meteorological data using BiLSTM was compared with satellite-derived NDVI. Whether the predicted NDVI is suitable for monitoring vegetation activity was validated using satellite-derived VCI. Specifically, both the spatial pattern and the time series values for NDVI and VCI were compared. For all kinds of comparison, the widely used metrics, the coefficient of determination ( $R^2$ ), was used for quantitative assessment:

$$R^2 = \frac{\sum_{i=1}^N (\hat{y}_i - \bar{y})^2}{\sum_{i=1}^N (y_i - \bar{y})^2}, \quad (12)$$

where  $N$  is the number of pixels;  $\hat{y}_i$  and  $y_i$  denote the estimated and reference values of pixel  $i$ , respectively; and  $\bar{y}$  denotes the mean of reference values.

## 4. Results

### 4.1. NDVI Predicted Using Vegetation-Type-Based BiLSTM

Figure 3 shows the simulation results of mean NDVI fluctuation of the six vegetation types from 2009 to 2017, that is, deciduous forest, evergreen forest, mixed forest, grassland, savannas, and croplands. The mean value of NDVI for each vegetation type was calculated based on 20 randomly selected samples. Annual NDVI fluctuation clearly varies from one vegetation type to another. The vegetation types of deciduous forest, grassland, savannas, and croplands have relatively stable year-to-year amplitudes compared to those of evergreen and mixed forests. Although apparent discrepancies exist, the NDVI–BiLSTM deep model can predict the NDVI time series of each vegetation type well. The predicted NDVI time series profiles are remarkably close to the satellite-derived profiles. For vegetation type with only one peak (such as deciduous forest, grassland, savannas, and croplands), the predicted NDVI has a very good consistency with the satellite-monitored NDVI in almost all years, especially the deciduous forest. As shown in Figure 3, evergreen and mixed forests often have complex profiles owing to plant growth or leaf senescence. The simulation values are somewhat worse than the four types above, whereas the results are desirable compared to satellite monitoring.

The growing season is important for vegetation growth, and is often defined as the daily temperature of  $5^\circ\text{C}$  lasting for more than 5 days [60]. In this study, we employed ten months from March to October as the growing season directly to investigate the agreement between the predicted NDVIs and ground truth. Figure 4 shows the mean NDVI of the growing season (March–October) throughout China. The mean monthly NDVI of each pixel is calculated using all the values in each month throughout the nine years. Figure 4 shows that the vegetation activities can be captured by our simulation method. The vegetation growth starts in March and peaks in August, and vegetation grows well in both central and southern China. Overall, the predicted NDVIs agree well with the ground truth derived from satellites in the view of the country range, and the seasonal change information about NDVI variation and trend are also well presented across months. It is slightly regrettable that the predicted results appear smoother than that of the ground truth with less detailed characteristics from the aspect of spatial distribution.

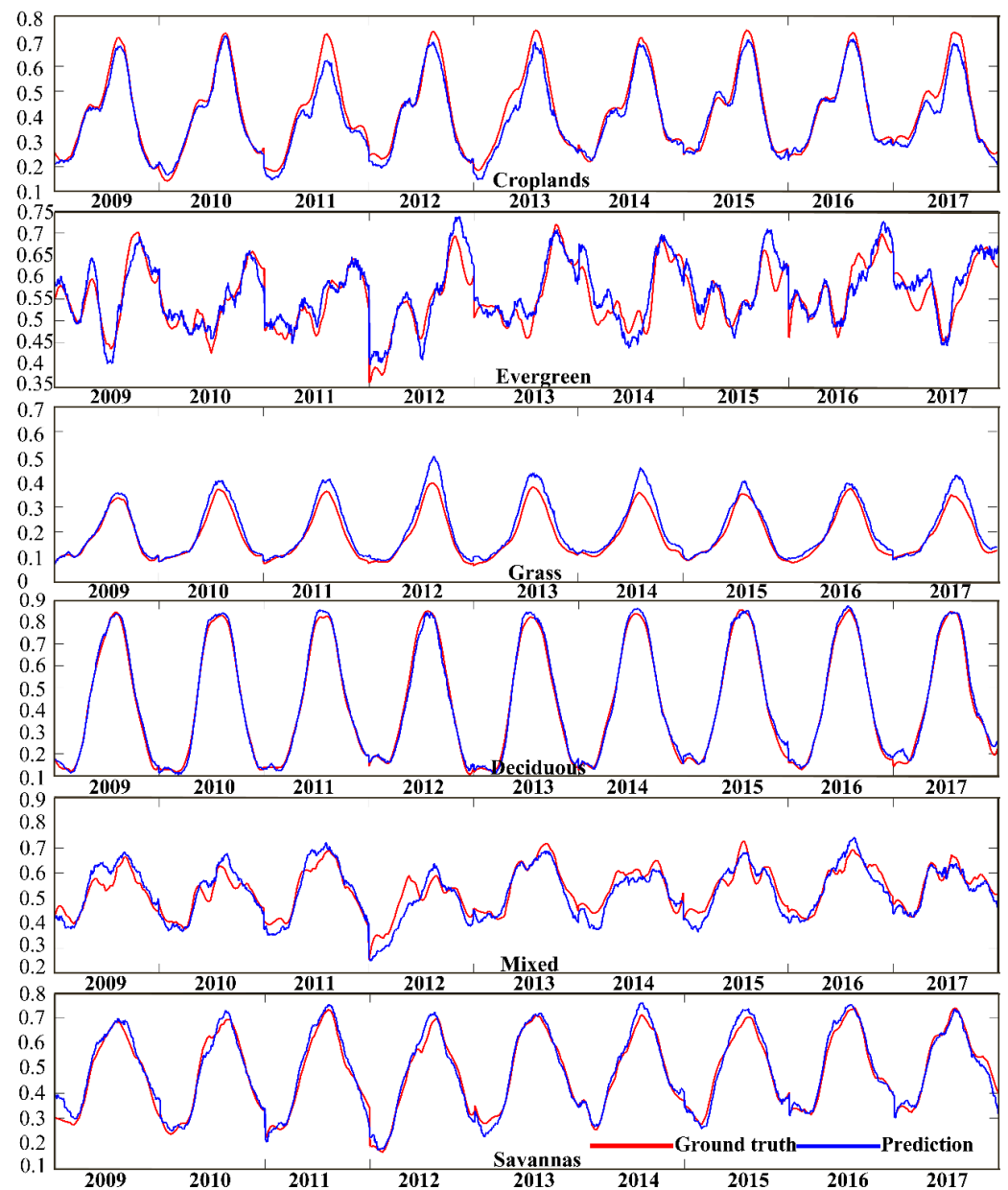


**Figure 3.** Mean NDVI for the 20 randomly selected samples of each vegetation type within the study area.

#### 4.2. Assessment of the NDVI Simulation

Figure 5 shows the performance of the 20 randomly selected pixels of each vegetation type over the years 2009–2017. The x-axis presents the ground truth and the y-axis the prediction. All  $R^2$  values of the six vegetation types are greater than 0.5. Specifically, the vegetation type of deciduous trees achieved the highest accuracy, followed by savannas, croplands, and grass, which is consistent with the previous results presented in Figure 3. The strongest predictions of NDVI are between 0.1–0.8 for croplands and deciduous, 0.4–0.9 for evergreen, 0–0.3 for grassland, 0.4–0.9 for mixed, and 0–0.9 for savannas. In other words, predictive performances are good for croplands, savannas, and deciduous as the strongest predictions covering almost the entire range of NDVI, that is, 0–1. Performance lowers for low NDVI values in evergreen and mixed forest and for high NDVI values in grasslands. The low predictive performance for high NDVI values in grasslands may be due to the overprediction of the peak NDVI values in grassland. As shown in Figure 3, the peak NDVI values of grassland are often centered at approximately 0.4–0.5, and our method may predict higher values than actual for high NDVI values. The drop in the accuracies

of evergreen and mixed forest at low NDVI values are probably because they often have high values in NDVI profiles, and our method achieves lower values than actual values. In terms of the two types, mixed forests have slightly better accuracy than evergreen forests.

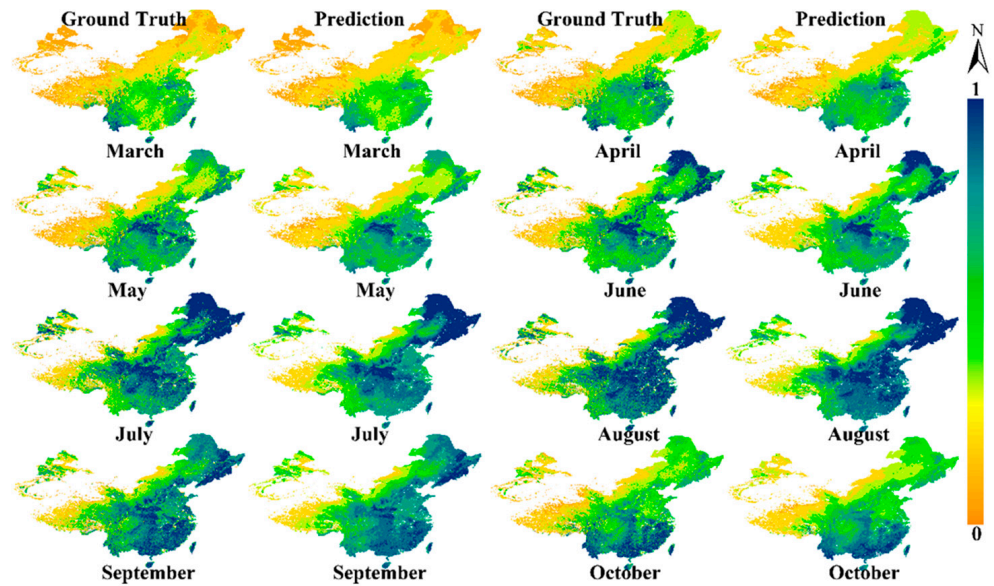


Figure 4. The mean NDVI values from March to October from 2009 to 2017. Both the ground truth and predicted NDVIs are presented. The first and third columns show the results of the ground truth derived from satellites, and the second and fourth columns are the predicted NDVIs.

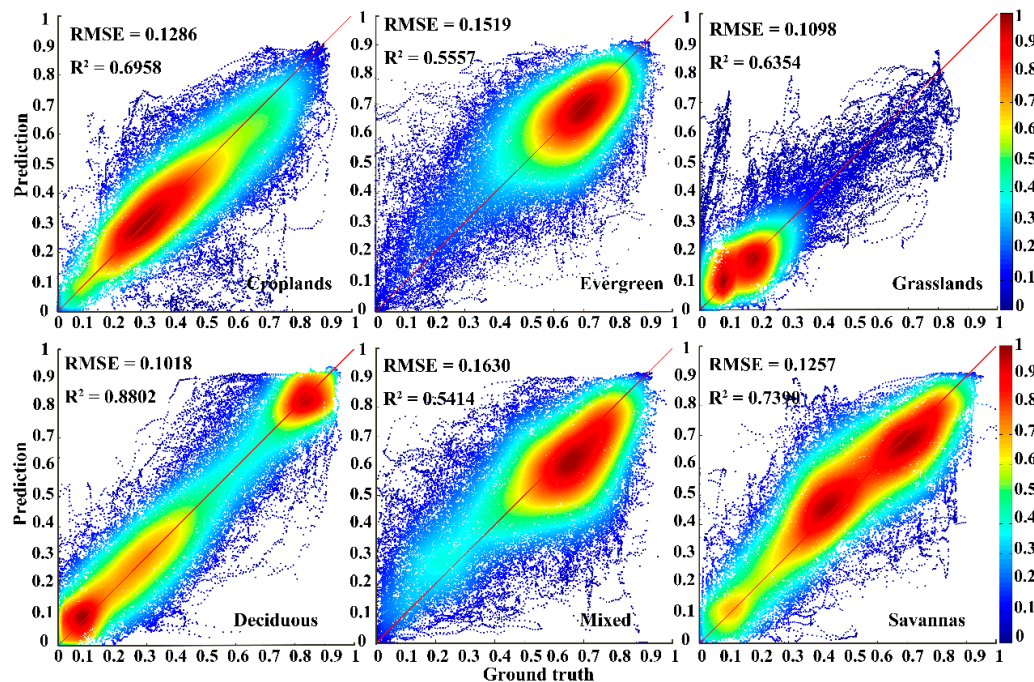
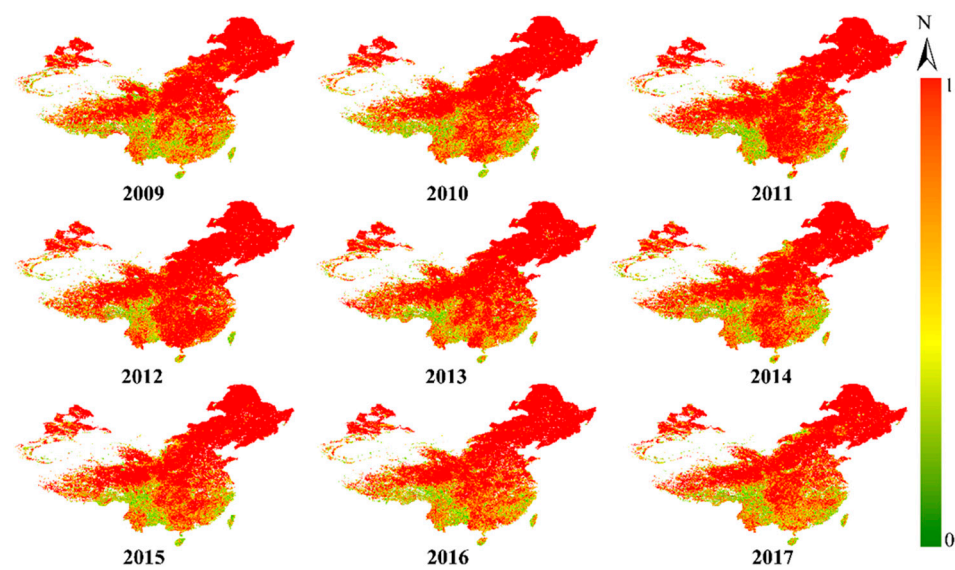


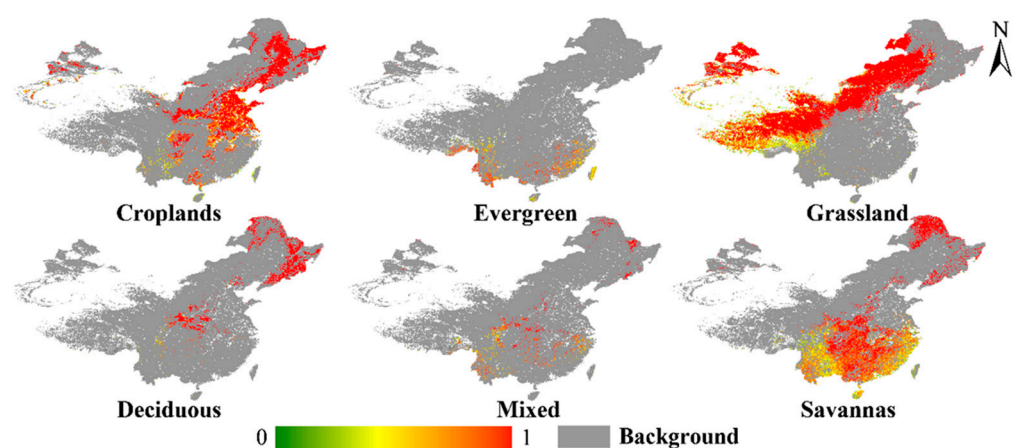
Figure 5. Performance across mean values of satellite measured and predicted NDVIs of the 20 randomly selected pixels for each vegetation type; the total number of NDVI values is 65700 in each density scatter plot.

We also assessed the performance of our method over the entire country. Figure 6 shows the yearly R<sup>2</sup> between the predicted NDVI values and the satellite-derived values. It is clear that the predicted NDVI has the strongest relationship with ground truth in the middle and north of the country, especially the northeast. The results in the southeast and

southwest vary in accuracy across different years, and the year 2012 has the highest  $R^2$  visually. Therefore,  $R^2$  values among the years range from  $0.66 \pm 0.29$  (2017) to  $0.75 \pm 0.35$  (2012) (See Table 1). The differences in performance are mainly because NDVI profiles often change with the weather instead of maintaining a monotonous consistency. The model may have some limitations owing to the training samples and can capture the change well in some years but not in others. To investigate the simulation results of each vegetation type, we visualized the mean  $R^2$  of each pixel in each vegetation type for the years 2009–2017 (Figure 7). Considering the entire country, we calculated the mean  $R^2$  of each vegetation type (Table 1). Compared with the results of 20 randomly selected samples (Figure 5), similar conclusions can be drawn from Figure 7, where the deciduous forest has the best simulation accuracy. The croplands and mixed forests are underestimated in the random sample assessment, whereas savannas are largely overestimated.



**Figure 6.** Yearly  $R^2$  of NDVIs between simulation and ground truth throughout China from 2009 to 2017. For each pixel, all the NDVI values in the days of a year are used for calculating  $R^2$ .

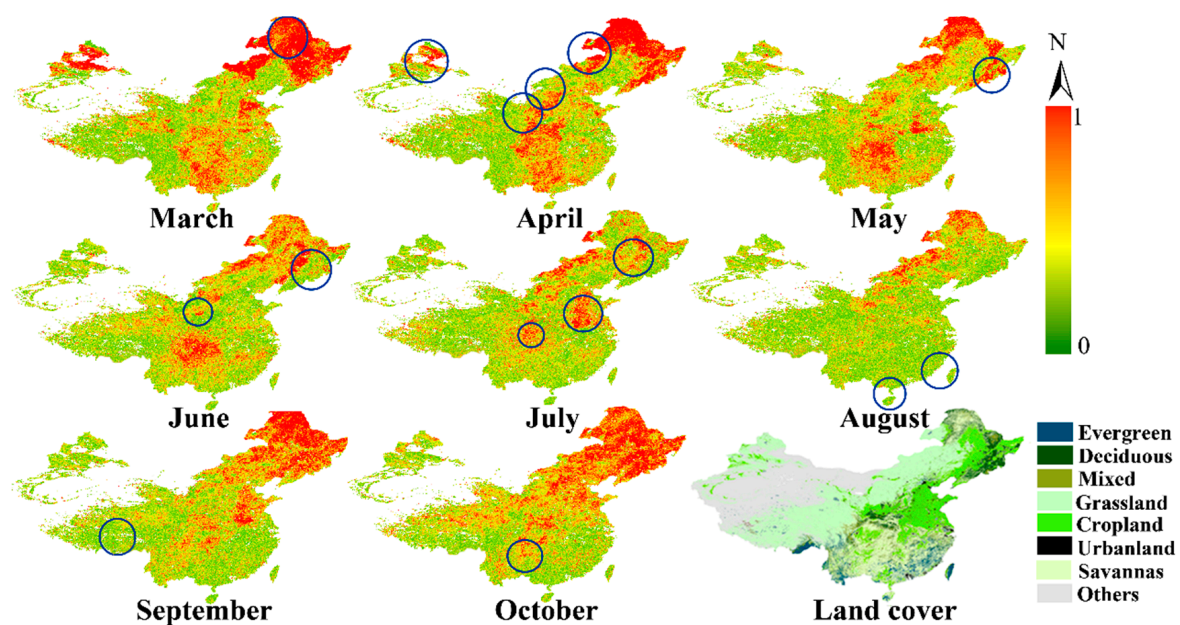


**Figure 7.** The  $R^2$  of NDVI between simulation and ground truth for each vegetation type throughout China from 2009 to 2017. For each pixel, all the NDVI values on each day during 2009–2017 are used for calculating  $R^2$ .

**Table 1.** Yearly mean NDVI throughout China from 2009 to 2017, as well as the mean NDVI of each vegetation type.

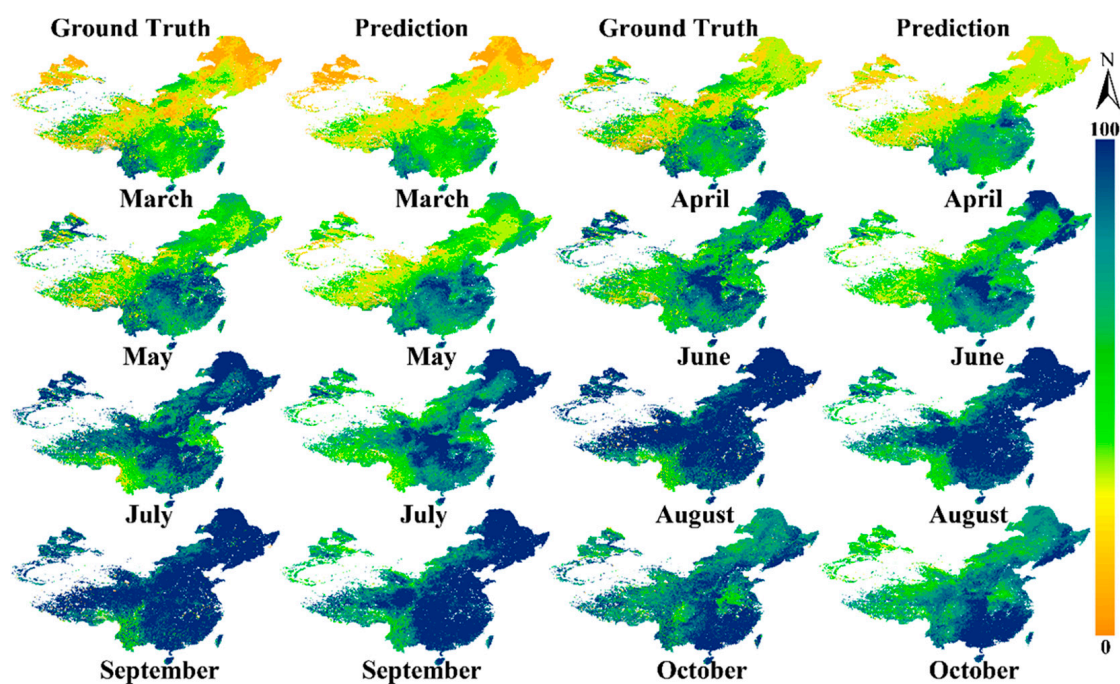
Year	NDVI	Vegetation Types	NDVI
2009	$0.66 \pm 0.29$	Croplands	$0.73 \pm 0.24$
2010	$0.70 \pm 0.28$	Deciduous	$0.87 \pm 0.16$
2011	$0.71 \pm 0.27$	Evergreen	$0.46 \pm 0.18$
2012	$0.75 \pm 0.25$	Grasslands	$0.67 \pm 0.28$
2013	$0.71 \pm 0.27$	Mixed	$0.61 \pm 0.23$
2014	$0.67 \pm 0.29$	Savannas	$0.59 \pm 0.24$
2015	$0.69 \pm 0.28$	—	—
2016	$0.68 \pm 0.28$	—	—
2017	$0.66 \pm 0.29$	—	—

Figure 8 shows the monthly R square between the predicted NDVI values and satellite-derived values of growing seasons across 2009–2017, which indicates the seasonal oscillations under different meteorological conditions. The spatial pattern in the variability of monthly R square varies with time and vegetation type, which corresponds to the vegetation phenological cycles. Savannas, grassland, and mixed forest marked on subfigures of March, April and May (the top three), respectively, have the strongest relationship between the predicted and satellite-derived values from March to October. The type of deciduous (circled in subfigure of June) has good accuracy over the growing season, except August and September, and croplands (circled in subfigure July) as well as grassland (the left one circled in subfigure April) also have the similar results. The type of evergreen distributed in bottom right (marked in subfigure August) has relative low R square, as it often has complex activities owing to the plant growth or leaf senescence. The model performances on grassland in the southern west and northern west (marked in subfigure September) are lower than grassland in other regions, which is probably due to the fact that the elevation is higher than that of the east, and the complex climate influences the vegetation activities. Beside these, the model performance is desirable on southern savannas (marked in subfigure October). In summary, although low R square values exist, the BiLSTM method can well capture the vegetation activity trend from the NDVI profiles (Figure 3) and NDVI maps (Figure 4) above.

**Figure 8.** R square between March–October satellite-derived NDVIs and predicted NDVIs. For each pixel, all the NDVI values in each month across 2009–2017 are used for R square calculation.

#### 4.3. Vegetation Activity and Stress Monitoring via Vegetation Condition Index

A full range of VCI in the growing season is shown in Figure 9 to obtain the vegetation activities. Taking China as a whole, the average VCI of each month during 2009–2017 is reported in Table 2. According to the average VCI, March and April exhibit a vegetation stress, especially in the northwest and northeast regions. This stress may be partly influenced by the growing season we used. As we defined above, we used months to define the growing season, during which the daily temperature may be lower than 5 °C for these regions in March and April, leading to vegetation stress. The vegetation condition is gradually favorable from March to October. Taking the country as a whole, the average VCI in the growing season is  $55 \pm 18$ , in comparison with the prediction of  $51 \pm 16$ . Thus, the satellite-derived ground truth and predicted VCI have similar results, showing a normal condition of vegetation growth. The VCI calculated from the predicted NDVI is lower than those of the satellite-derived ground truth, which is probably because our method may have underestimated the NDVI values when considering all six vegetation types together. As shown in Figure 9, the predicted VCI values in the middle and northwest regions of the country are lower than those of the ground truth.



**Figure 9.** The mean VCI values from March to October during 2009–2017. Both the ground truth and predicted VCIs are presented. The first and third columns show the results of the ground truth derived from satellites, and the second and fourth columns are the predicted VCIs.

**Table 2.** The average VCI of whole China during growing season from March to October from 2009 to 2017.

	March	April	May	June	July	August	September	October	Average
GT	$27 \pm 17$	$35 \pm 18$	$45 \pm 18$	$54 \pm 18$	$65 \pm 18$	$76 \pm 16$	$75 \pm 14$	$63 \pm 14$	$55 \pm 18$
Prediction	$25 \pm 15$	$33 \pm 15$	$42 \pm 16$	$50 \pm 16$	$59 \pm 17$	$70 \pm 16$	$70 \pm 14$	$58 \pm 14$	$51 \pm 16$

On filtering nonweather effects using geographic filtering, yearly mean VCI shows a slightly better  $R^2$  than NDVI (Figure 10; Table 3). The vegetation activities predicted by meteorological data in most of China have strong consistency with those monitored by satellite. Similar to the above results (Figure 6), grasslands in the southwest and savannas in the southeast and southwest have slightly lower simulation results. These areas are

often located in the Qinghai Tibet Plateau, as well as the subtropical or tropical region, with complex climatic conditions. If we use three ranges (stress, normal, and favorable) to describe vegetation activity, the VCI calculated using predicted NDVI is a good alternative.

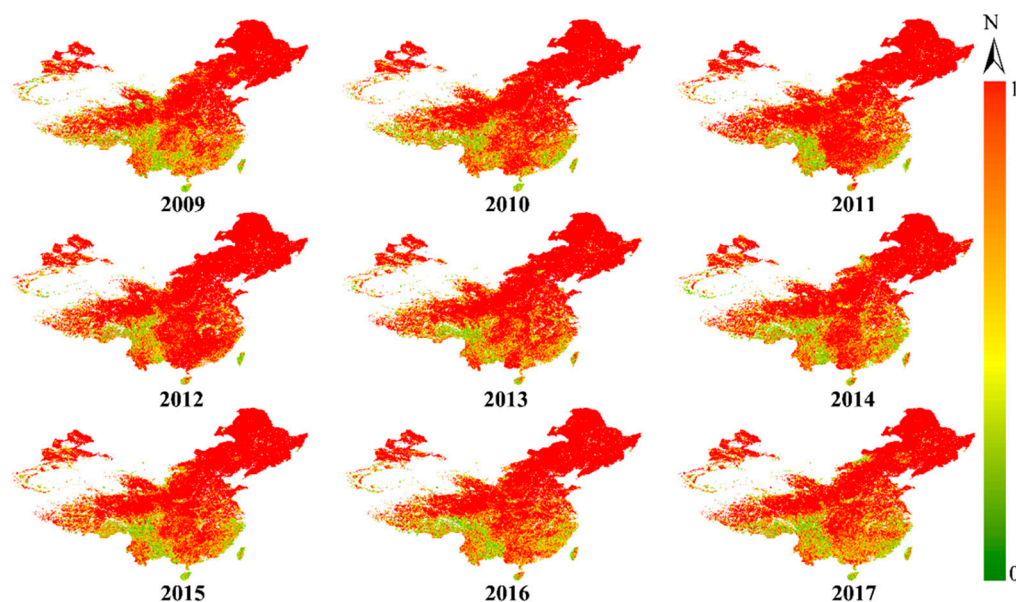


**Figure 10.** Yearly mean  $R^2$  of VCI calculated by the predicted NDVI throughout China from 2009 to 2017. For each pixel, all the VCI values in the days of a year are used for calculating  $R^2$ .

**Table 3.** Yearly mean  $R^2$  between the predicted and satellite-derived VCI throughout China from 2009 to 2017.

Year	2009	2010	2011	2012	2013
$R^2$	$0.67 \pm 0.29$	$0.70 \pm 0.28$	$0.72 \pm 0.27$	$0.75 \pm 0.25$	$0.72 \pm 0.27$
Year	2014	2015	2016	2017	
$R^2$	$0.68 \pm 0.29$	$0.70 \pm 0.28$	$0.69 \pm 0.28$	$0.67 \pm 0.29$	

#### 4.4. Trends in Vegetation drought in China across 2008–2017

We also analyzed the trends of vegetation activities in China during the period 2008–2017. Figure 11 shows the trend of vegetation activity using Sen's slope and MK test. In this study, the length of the time series is about 470 weeks (2009–2017), and the test statistic MK is used for trend significance analysis and slope for magnitude calculation. Given the significance level  $\alpha = 0.05$ ,  $MK_{1-\alpha/2} = MK_{0.975} = 1.96$ , we found that there is no pixel that satisfies Sen's slope  $> 0$  and  $|MK| > 1.96$ , and Sen's slope  $< 0$  and  $|MK| > 1.96$ . Namely, there is no vegetation type that shows a marked improvement or marked degradation. Throughout the whole country, an obvious upward but not significant trend is displayed, that is, a slight improvement (see the black pixels). Statistically, 98.51% of the vegetation over the country is slightly improved, in comparison with 95.74% of the predicted value. The inconsistencies between the ground truth and simulation in Figure 11 lie in the northwest (circled with blue, mainly grasslands), middle west, and middle east (circled with orange, covered with savannas or evergreen forests).

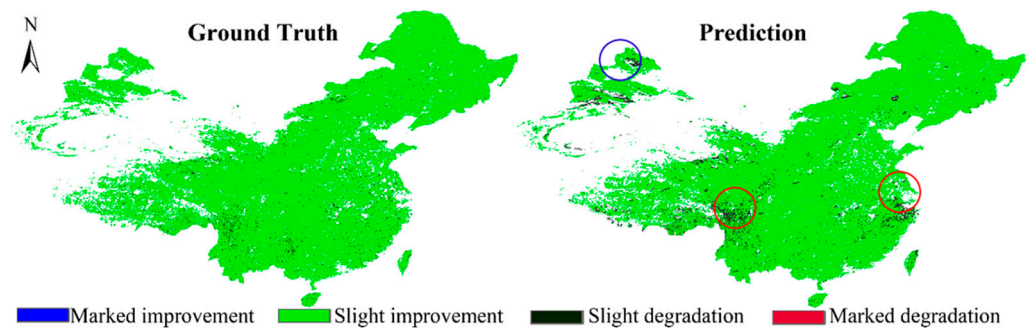


**Figure 11.** The comparison of trends for vegetation activities in China during 2008–2017.

## 5. Discussion

Deep learning architecture that influences NDVI simulation: For NDVI simulation, we tested several LSTM architectures to obtain the best performance. Figure 12 shows the performances of three different architectures: LSTM, BiLSTM-2layers and BiLSTM-3layers. The LSTM (yellow line) has the largest gap with GT which is derived from the satellite images among May and July. Both BiLSTM architectures provide better accuracies than LSTM except for August, indicating that the NDVI prediction benefits from both the forward and backward directions. The number of layers also influences the simulation accuracy. As many studies have reported, deep architectures are helpful for time series prediction. However, we found that the three-layer BiLSTM is sensitive to meteorological data, and the result (green line) is not as smooth as the result of the two-layer one (blue line). Moreover, the gap between the three-layer BiLSTM and GT is larger than that between the two-layer BiLSTM and GT, meaning that the two-layer BiLSTM architecture produces the least error over the time series. It is proven that it is worth considering both the forward and the backward directions of time series in prediction as well as the length of the network in temporal feature learning.

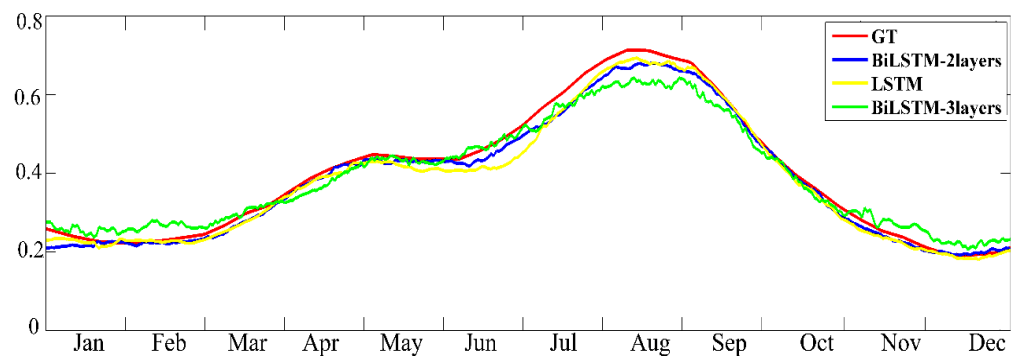


**Figure 12.** The performances of LSTM, BiLSTM-2layers, and BiLSTM-3layers on NDVI simulation.

Figure 13 shows the sensitivity of NDVI simulation to meteorological variables: To quantify the impacts of meteorological variables on NDVI simulation, we explored the simulation sensitivity of the six vegetation types to the meteorological variables. Although the vegetation phenological cycles vary with six vegetation types, the vegetation types—except evergreen—showed similar sensitivity to meteorological variables in NDVI simulation. The meteorological variables, maximum air temperature, and minimum air temperature had the greatest impact on the NDVI simulation. This is consistent with our consideration that air temperature correlated strongly with vegetation growth, followed by day length and precipitation. Although air temperature was an important impact factor for evergreen, the  $R^2$  was lower than that of other vegetation types. The reason may be that evergreen forests are often distributed in subtropical and tropical areas, and that the air temperature is sufficient. Comparatively, day length is the most important factor that influences evergreen

growth. Because of the low relationships between meteorological variables and evergreen, other factors may be included in the evergreen NDVI simulation in a future study.

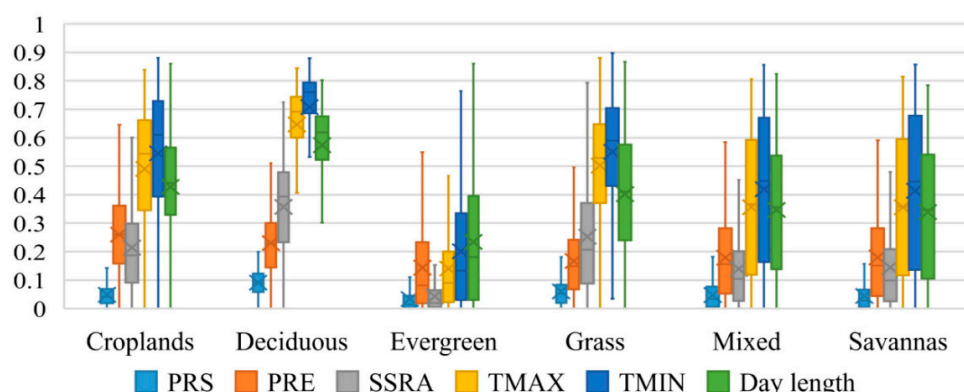


**Figure 13.** The sensitivity of NDVI simulation to meteorological variables across six vegetation types. Y axis reports  $R^2$  between the meteorological variables and NDVI. PRS, PRE, SSRA, TMAX, TMIN denote atmospheric pressure, precipitation, incoming shortwave radiation, maximum air temperature, and minimum air temperature, respectively.

**BiLSTM abilities to NDVI simulation and vegetation activity monitoring:** The performances of our one-model method are similar to the GAM and ANN-mixed model in the work of Adede et al. [32], which used precipitation and vegetation indices as the input variables. However, they only predict 3 months of vegetation conditions. Our method can conduct the prediction at an arbitrary time scale as long as the future meteorological data are available. Zhou et al. [28] employed a multi-regression model for NDVI prediction based on precipitation and  $ET_0$ . Our prediction results on the validation dataset are comparable with their prediction results on the base period (they selected training data for this period). The R square on the validation period was not reported in their work, and the accuracy on the validation dataset is often lower than that on the training dataset. For vegetation activity monitoring, we compared the relative studies about the drought event in China. In the works of Li et al. [61] and Song et al. [62], the impacts of 2009–2010 Southwestern China winter-spring drought on vegetation were investigated. Here, we visualized the predicted monthly NDVI from September 2009 to May 2010 (Figure 14). It can be seen that the predicted NDVI based on our method agrees well with the spatial pattern of their works, indicating a potential vegetation drought prediction method. The results can provide reference for the early warning of drought to the policy maker and help the management of regional vegetation growth. Governments can develop policies in advance to protect vegetation in areas that may be at risk of drought and reduce vegetation damage and ecological loss.

In general, vegetation-type-based BiLSTM–NDVI prediction using meteorological data is a good alternative for satellite monitoring. For the six vegetation types, the model performs best in vegetated areas such as deciduous forests, croplands, and grasslands. It is encouraging that the model performs well in croplands, even though we did not account for anthropic activities. This means that the model makes it possible to forecast drought. Spatially, better performances are obtained in northern China than in regions with complex climate conditions and topography, that is, southern China as well as the Qinghai Tibet Plateau. In terms of monitoring vegetation activity, the VCI derived from the deep learning method is similar to that derived from satellite data. When classifying vegetation conditions into three categories based on the VCI values—that is, stressed, normal, and favorable—as the target, the proposed method produces results that are comparable to the satellite-derived results. All these results indicate that deep learning methods could play an important role in identifying potential vegetation stress using meteorological data.

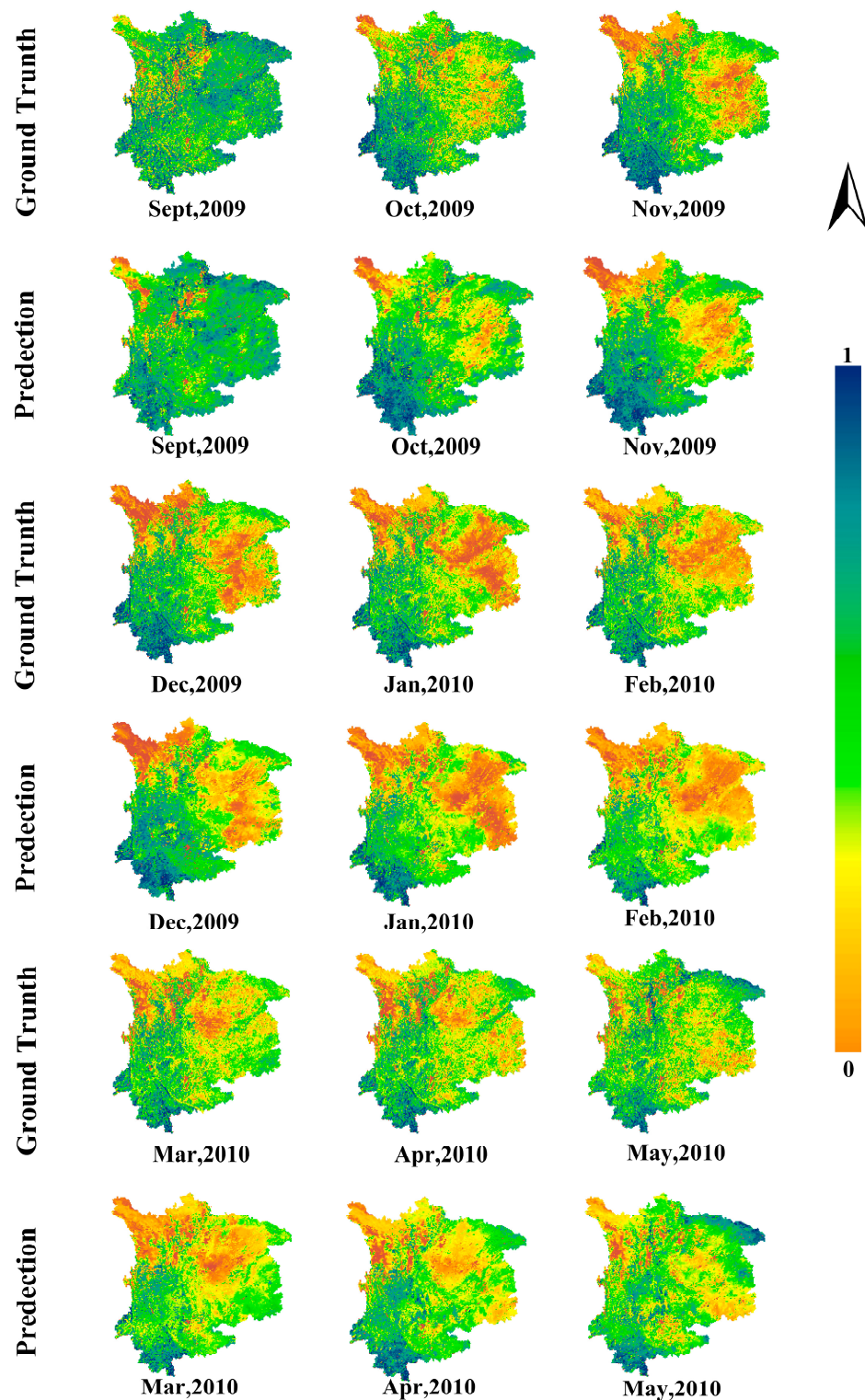


Figure 14. The impacts of 2009–2010 Southwestern China winter-spring drought on vegetation.

## 6. Conclusions

In this paper, we proposed a vegetation-type-based BiLSTM method for simulating NDVI time series based on meteorological data. The experimental results indicate the feasibility of using BiLSTM and meteorological data for simulating NDVI time series for each vegetation type. The long-term memory of the LSTM unit can effectively store information on temporal time series. The mean  $R^2$  value between the BiLSTM-predicted and satellite-derived NDVI was  $0.69 \pm 0.28$ . Among the six studied vegetation types, vegetation-

type-based BiLSTM achieved the best accuracy in deciduous forests  $R^2 = 0.87 \pm 0.16$ . One possible reason is that deciduous forests have a relatively simple temporal profile that corresponds to vegetation phenology cycles. We further used the predicted NDVI to monitor vegetation conditions and stresses in response to climate-related factors using the VCI. Both model-predicted and satellite-derived VCIs can detect similar spatial patterns of vegetation stresses with a mean  $R^2$  of  $0.70 \pm 0.28$ . We also found that vegetation activity showed an upward, but insignificant, trend in the past decade.

Our study demonstrated the potential of using meteorological data for NDVI simulation based on deep learning, not only useful for retrospective analysis, but it also has the ability for future prediction. Moreover, the model can be used to monitor vegetation type-based stresses using meteorological data, which could successfully reproduce the behavior of vegetation activities and stresses under varied climate conditions, as compared with remote sensing data.

**Author Contributions:** Conceptualization, Y.S.; Methodology, Y.S. and D.L.; Investigation, D.L.; Resources, D.L.; Data curation, Y.R.; Writing—original draft, Y.S.; Writing—review & editing, C.H.; Visualization, Y.R.; Supervision, Q.X.; Project administration, Q.X.; Funding acquisition, Y.S. and Q.X. All authors have read and agreed to the published version of the manuscript.

**Funding:** This research was supported by the National Natural Science Foundation of China (grant nos. 42171308 and 41875122), Natural Science Foundation of Guangdong Province (grant no. 2021A1515011429), the National Key R&D Program of China (grant nos. 2017YFA0604300 and 2017YFA0604400), Western Talent (grant no. 2018XBYJRC004), and Guangdong Top Young Talents of Science and Technology (grant no. 2017TQ04Z359). We thank the anonymous reviewers for their constructive comments.

**Institutional Review Board Statement:** Not applicable.

**Informed Consent Statement:** Not applicable.

**Data Availability Statement:** The meteorological data of CLDAS used in this study are available at [http://data.cma.cn/data/detail/dataCode/NAFP\\_CLDAS2.0\\_RT.html](http://data.cma.cn/data/detail/dataCode/NAFP_CLDAS2.0_RT.html) (accessed on 20 April 2020). The remote sensing data (MOD09A1 and MCD12Q1) are available at <https://lpdaac.usgs.gov/data/> (accessed on 5 April 2023). The experimental codes are available at <https://github.com/sunying23/vegetation-BiLSTM> (accessed on 5 April 2023).

**Conflicts of Interest:** The authors declare no conflict of interest.

## References

- Xu, L.; Abbaszadeh, P.; Moradkhani, H.; Chen, N.; Zhang, X. Continental drought monitoring using satellite soil moisture, data assimilation and an integrated drought index. *Remote Sens. Environ.* **2020**, *250*, 112028. [CrossRef]
- Gao, J.; Jiao, K.; Wu, S.; Ma, D.; Zhao, D.; Yin, Y.; Dai, E. Past and future effects of climate change on spatially heterogeneous vegetation activity in China. *Earth's Future* **2017**, *5*, 679–692. [CrossRef]
- Peng, S.-S.; Piao, S.; Zeng, Z.; Ciais, P.; Zhou, L.; Li, L.Z.X.; Myneni, R.B.; Yin, Y.; Zeng, H. Afforestation in China cools local land surface temperature. *Proc. Natl. Acad. Sci. USA* **2014**, *111*, 2915–2919. [CrossRef]
- Piao, S.; Tan, K.; Nan, H.; Ciais, P.; Fang, J.; Wang, T.; Vuichard, N.; Zhu, B. Impacts of climate and CO<sub>2</sub> changes on the vegetation growth and carbon balance of Qinghai–Tibetan grasslands over the past five decades. *Glob. Planet. Change* **2012**, *98–99*, 73–80. [CrossRef]
- Reddy, D.S.; Prasad, P.R.C. Prediction of vegetation dynamics using NDVI time series data and LSTM. *Model. Earth Syst. Environ.* **2018**, *4*, 409–419. [CrossRef]
- Chen, B.; Xu, G.; Coops, N.C.; Ciais, P.; Innes, J.L.; Wang, G.; Myneni, R.B.; Wang, T.; Krzyzanowski, J.; Li, Q.; et al. Changes in vegetation photosynthetic activity trends across the Asia–Pacific region over the last three decades. *Remote Sens. Environ.* **2014**, *144*, 28–41. [CrossRef]
- Stepchenko, A.; Chizhov, J. NDVI Short-Term Forecasting Using Recurrent Neural Networks. *Environment. Technology. Resources. Proc. Int. Sci. Pract. Conf.* **2015**, *3*, 180. [CrossRef]
- Ali, S.; Zhang, H.; Qi, M.; Liang, S.; Ning, J.; Jia, Q.; Hou, F. Monitoring drought events and vegetation dynamics in relation to climate change over mainland China from 1983 to 2016. *Environ. Sci. Pollut. Res.* **2021**, *28*, 21910–21925. [CrossRef]
- Rouse, J.W.; Haas, R.H.; Schell, J.A.; Deering, D.W.; Haas, R.H.; Schell, J.A.; Deering, D.W. Monitoring vegetation systems in the Great Plains with ERTS. In *Third Earth Resources Technology Satellite-1 Symposium- Volume I: Technical Presentations, Greenbelt, MD, United States*; NASA: Washington, DC, USA, 1974; p. 309.

10. Gitelson, A.A.; Kaufman, Y.J.; Merzlyak, M.N. Use of a green channel in remote sensing of global vegetation from EOS-MODIS. *Remote Sens. Environ.* **1996**, *58*, 289–298. [[CrossRef](#)]
11. Delegido, J.; Verrelst, J.; Meza, C.M.; Rivera, J.P.; Alonso, L.; Moreno, J. A red-edge spectral index for remote sensing estimation of green LAI over agroecosystems. *Eur. J. Agron.* **2013**, *46*, 42–52. [[CrossRef](#)]
12. Huete, A.R. A soil-adjusted vegetation index (SAVI). *Remote Sens. Environ.* **1988**, *25*, 295–309. [[CrossRef](#)]
13. Huete, A.; Didan, K.; Miura, T.; Rodriguez, E.P.; Gao, X.; Ferreira, L.G. Overview of the radiometric and biophysical performance of the MODIS vegetation indices. *Remote Sens. Environ.* **2002**, *83*, 195–213. [[CrossRef](#)]
14. Chu, H.; Venevsky, S.; Wu, C.; Wang, M. NDVI-based vegetation dynamics and its response to climate changes at Amur-Heilongjiang River Basin from 1982 to 2015. *Sci. Total Environ.* **2019**, *650*, 2051–2062. [[CrossRef](#)]
15. Aban, J.; Tateishi, R.; Tsolmon, R. The Polynomial Least Squares Operation (PoLeS): A Method for Reducing Noise in NDVI Time Series Data. In Proceedings of the Asian Conference on Remote Sensing (ACRS 2002), Kathmandu, Nepal, 25–29 November 2002.
16. Petitjean, F.; Inglada, J.; Gancarski, P. Assessing the quality of temporal high-resolution classifications with low-resolution satellite image time series. *Int. J. Remote Sens.* **2014**, *35*, 2693–2712. [[CrossRef](#)]
17. Zhao, S.; Cong, D.; He, K.; Yang, H.; Qin, Z. Spatial-Temporal Variation of Drought in China from 1982 to 2010 Based on a modified Temperature Vegetation Drought Index (mTVDI). *Sci. Rep.* **2017**, *7*, 17473. [[CrossRef](#)]
18. Jiang, Y.; Ranghai, W.; Peng, Q.; Wu, X.; Ning, H.; Li, C. The relationship between drought activity and vegetation cover in Northwest China from 1982 to 2013. *Nat. Hazards* **2018**, *92*, 145–163. [[CrossRef](#)]
19. Kogan, F.N. Global Drought Watch from Space. *Bull. Am. Meteorol. Soc.* **1997**, *78*, 621–636. [[CrossRef](#)]
20. Liang, L.; Qiu, S.; Yan, J.; Shi, Y.; Geng, D. VCI-Based Analysis on Spatiotemporal Variations of Spring Drought in China. *Int. J. Environ. Res. Public Health* **2021**, *18*, 7967. [[CrossRef](#)]
21. Liu, L.; Liao, J.; Chen, X.; Zhou, G.; Su, Y.; Xiang, Z.; Wang, Z.; Liu, X.; Li, Y.; Wu, J.; et al. The Microwave Temperature Vegetation Drought Index (MTVDI) based on AMSR-E brightness temperatures for long-term drought assessment across China (2003–2010). *Remote Sens. Environ.* **2017**, *199*, 302–320. [[CrossRef](#)]
22. Nay, J.; Burchfield, E.; Gilligan, J. A machine-learning approach to forecasting remotely sensed vegetation health. *Int. J. Remote Sens.* **2018**, *39*, 1800–1816. [[CrossRef](#)]
23. Mazza, A.; Gargiulo, M.; Scarpa, G.; Gaetano, R. Estimating the NDVI from SAR by Convolutional Neural Networks. In Proceedings of the IGARSS 2018-2018 IEEE International Geoscience and Remote Sensing Symposium, Valencia, Spain, 22–27 July 2018; pp. 1954–1957.
24. Wright, C.K.; de Beurs, K.M.; Henebry, G.M. Combined analysis of land cover change and NDVI trends in the Northern Eurasian grain belt. *Front. Earth Sci.* **2012**, *6*, 177–187. [[CrossRef](#)]
25. Wu, Y.; Tang, G.; Gu, H.; Liu, Y.; Yang, M.; Sun, L. The variation of vegetation greenness and underlying mechanisms in Guangdong province of China during 2001–2013 based on MODIS data. *Sci. Total Environ.* **2019**, *653*, 536–546. [[CrossRef](#)] [[PubMed](#)]
26. Wang, T.; Lin, X.; Liu, Y.; Dantec-Nédélec, S.; Otlé, C. Causes of uncertainty in China’s net primary production over the 21st century projected by the CMIP5 Earth system models. *Int. J. Climatol.* **2016**, *36*, 2323–2334. [[CrossRef](#)]
27. Zheng, Y.; Han, J.; Huang, Y.; Fassnacht, S.R.; Xie, S.; Lv, E.; Chen, M. Vegetation response to climate conditions based on NDVI simulations using stepwise cluster analysis for the Three-River Headwaters region of China. *Ecol. Indic.* **2018**, *92*, 18–29. [[CrossRef](#)]
28. Zhou, Z.; Ding, Y.; Shi, H.; Cai, H.; Fu, Q.; Liu, S.; Li, T. Analysis and prediction of vegetation dynamic changes in China: Past, present and future. *Ecol. Indic.* **2020**, *117*, 106642. [[CrossRef](#)]
29. Barrett, A.; Duivenvoorden, S.; Salakpi, E.; Muthoka, J.; Mwangi, J.; Oliver, S.; Rowhani, P. Forecasting vegetation condition for drought early warning systems in pastoral communities in Kenya. *Remote Sens. Environ.* **2020**, *248*, 111886. [[CrossRef](#)]
30. Han, J.-C.; Huang, Y.; Zhang, H.; Wu, X. Characterization of elevation and land cover dependent trends of NDVI variations in the Hexi region, northwest China. *J. Environ. Manag.* **2019**, *232*, 1037–1048. [[CrossRef](#)]
31. Forkel, M.; Dorigo, W.; Lasslop, G.; Teubner, I.; Chuvieco, E.; Thonicke, K. A data-driven approach to identify controls on global fire activity from satellite and climate observations (SOFIA V1). *Geosci. Model Dev.* **2017**, *10*, 4443–4476. [[CrossRef](#)]
32. Adede, C.; Oboko, R.; Wagacha, P.W.; Atzberger, C. A Mixed Model Approach to Vegetation Condition Prediction Using Artificial Neural Networks (ANN): Case of Kenya’s Operational Drought Monitoring. *Remote Sens.* **2019**, *11*, 1099. [[CrossRef](#)]
33. Kamilaris, A.; Prenafeta-Boldú, F.X. Deep learning in agriculture: A survey. *Comput. Electron. Agric.* **2018**, *147*, 70–90. [[CrossRef](#)]
34. Das, M.; Ghosh, S.K. Deep-STEP: A Deep Learning Approach for Spatiotemporal Prediction of Remote Sensing Data. *IEEE Geosci. Remote Sens. Lett.* **2016**, *13*, 1984–1988. [[CrossRef](#)]
35. Su, B.; Lu, S. Accurate Recognition of Words in Scenes without Character Segmentation Using Recurrent Neural Network. *Pattern Recognit.* **2017**, *63*, 397–405. [[CrossRef](#)]
36. Bahdanau, D.; Cho, K.; Bengio, Y. Neural Machine Translation by Jointly Learning to Align and Translate. *arXiv* **2016**. [[CrossRef](#)]
37. Cheng, J.; Dong, L.; Lapata, M. Long Short-Term Memory-Networks for Machine Reading. *arXiv* **2016**. [[CrossRef](#)]
38. Hochreiter, S.; Schmidhuber, J. Long short-term memory. *Neural Comput.* **1997**, *9*, 1735–1780. [[CrossRef](#)]
39. Venugopalan, S.; Hendricks, L.A.; Mooney, R.; Saenko, K. Improving LSTM-based Video Description with Linguistic Knowledge Mined from Text. *arXiv* **2016**, arXiv:1604.01729.

40. Zhong, L.; Hu, L.; Zhou, H. Deep learning based multi-temporal crop classification. *Remote Sens. Environ.* **2019**, *221*, 430–443. [[CrossRef](#)]
41. Lai, D.; Qi, Y.; Liu, J.; Dai, X.; Zhao, L.; Wei, S. Ventilation behavior in residential buildings with mechanical ventilation systems across different climate zones in China. *Build. Environ.* **2018**, *143*, 679–690. [[CrossRef](#)]
42. Chen, J.; Cao, X.; Peng, S.; Ren, H. Analysis and Applications of GlobeLand30: A Review. *ISPRS Int. J. Geo-Inf.* **2017**, *6*, 230. [[CrossRef](#)]
43. Chen, C.; Park, T.; Wang, X.; Piao, S.; Xu, B.; Chaturvedi, R.K.; Fuchs, R.; Brovkin, V.; Ciaia, P.; Fensholt, R.; et al. China and India lead in greening of the world through land-use management. *Nat. Sustain.* **2019**, *2*, 122–129. [[CrossRef](#)]
44. Amthor, J. Calculation of daylength. *Comput. Appl. Biosci. CABIOS* **1997**, *13*, 479–480. [[CrossRef](#)]
45. Vermote, E. *MODIS/Terra Surface Reflectance 8-Day L3 Global 500 m SIN Grid V061*; NASA EOSDIS Land Processes DAAC: Missoula, MT, USA, 2021. [[CrossRef](#)]
46. Chen, J.; Jönsson, P.; Tamura, M.; Gu, Z.; Matsushita, B.; Eklundh, L. A simple method for reconstructing a high-quality NDVI time-series data set based on the Savitzky–Golay filter. *Remote Sens. Environ.* **2004**, *91*, 332–344. [[CrossRef](#)]
47. Gray, J.; Sulla-Menashe, D.; Friedl, M.A. *User Guide to Collection 6 MODIS Land Cover Dynamics (MCD12Q2) Product*; NASA EOSDIS Land Processes DAAC: Missoula, MT, USA, 2019.
48. Loveland, T.R.; Belward, A.S. The International Geosphere Biosphere Programme Data and Information System global land cover data set (DIScover). *Acta Astronaut.* **1997**, *41*, 681–689. [[CrossRef](#)]
49. Unganai, L.S.; Kogan, F.N. Drought Monitoring and Corn Yield Estimation in Southern Africa from AVHRR Data. *Remote Sens. Environ.* **1998**, *63*, 219–232. [[CrossRef](#)]
50. Graves, A.; Mohamed, A.-r.; Hinton, G. Speech recognition with deep recurrent neural networks. In Proceedings of the 2013 IEEE International Conference on Acoustics, Speech and Signal Processing, Vancouver, BC, Canada, 26–31 May 2013; pp. 6645–6649.
51. Norman, S.P.; Koch, F.H.; Hargrove, W.W. Review of broad-scale drought monitoring of forests: Toward an integrated data mining approach. *For. Ecol. Manag.* **2016**, *380*, 346–358. [[CrossRef](#)]
52. Ghaeini, R.; Hasan, S.A.; Datla, V.; Liu, J.; Lee, K.; Qadir, A.; Ling, Y.; Prakash, A.; Fern, X.Z.; Farri, O. Dr-bilstm: Dependent reading bidirectional lstm for natural language inference. *arXiv* **2018**. [[CrossRef](#)]
53. Chollet, F.; Lorenzen, K. *Deep Learning mit Python und Keras: Das Praxis-Handbuch vom Entwickler der Keras-Bibliothek*; MITP: Frechen, Germany, 2018.
54. Srivastava, N.; Hinton, G.; Krizhevsky, A.; Sutskever, I.; Salakhutdinov, R. Dropout: A simple way to prevent neural networks from overfitting. *J. Mach. Learn. Res.* **2014**, *15*, 1929–1958.
55. Pei, F.; Wu, C.; Liu, X.; Li, X.; Yang, K.; Zhou, Y.; Wang, K.; Xu, L.; Xia, G. Monitoring the vegetation activity in China using vegetation health indices. *Agric. For. Meteorol.* **2018**, *248*, 215–227. [[CrossRef](#)]
56. Sen, P.K. Estimates of the Regression Coefficient Based on Kendall’s Tau. *J. Am. Stat. Assoc.* **1968**, *63*, 1379–1389. [[CrossRef](#)]
57. Mann, H.B. Nonparametric Tests Against Trend. *Econometrica* **1945**, *13*, 245–259. [[CrossRef](#)]
58. Kendall, M.G. *Rank Correlation Methods*; Griffin: London, UK, 1973; p. 399.
59. Gocic, M.; Trajkovic, S. Analysis of changes in meteorological variables using Mann-Kendall and Sen’s slope estimator statistical tests in Serbia. *Glob. Planet. Change* **2013**, *100*, 172–182. [[CrossRef](#)]
60. Linderholm, H.W. Growing season changes in the last century. *Agric. For. Meteorol.* **2006**, *137*, 1–14. [[CrossRef](#)]
61. Li, X.; Li, Y.; Chen, A.; Gao, M.; Slette, I.; Piao, S. The impact of the 2009/2010 drought on vegetation growth and terrestrial carbon balance in Southwest China. *Agric. For. Meteorol.* **2019**, *269*, 239–248. [[CrossRef](#)]
62. Song, L.; Li, Y.; Ren, Y.; Wu, X.; Guo, B.; Tang, X.; Shi, W.; Ma, M.; Han, X.; Zhao, L. Divergent vegetation responses to extreme spring and summer droughts in Southwestern China. *Agric. For. Meteorol.* **2019**, *279*, 107703. [[CrossRef](#)]

**Disclaimer/Publisher’s Note:** The statements, opinions and data contained in all publications are solely those of the individual author(s) and contributor(s) and not of MDPI and/or the editor(s). MDPI and/or the editor(s) disclaim responsibility for any injury to people or property resulting from any ideas, methods, instructions or products referred to in the content.